

2407 **Chapter 9**
2408 **Weak Focusing Synchrotron**

2409 **Abstract** This Chapter introduces to the weak focusing synchrotron, and to the the-
2410 oretical material needed for the simulation exercises. It begins with a brief reminder
2411 of the historical context, and continues with beam optics and acceleration techniques
2412 which the weak synchrotron principle and methods lean on. Regarding the latter, it
2413 relies on basic charged particle optics and acceleration concepts introduced in the
2414 previous Chapters, and further addresses the following aspects:

- 2415 - fixed closed orbit,
- 2416 - periodic structure,
- 2417 - periodic motion stability,
- 2418 - optical functions,
- 2419 - synchrotron motion,
- 2420 - depolarizing resonances.

2421 The simulation of weak synchrotrons only require a very limited number of optical
2422 elements; actually two are enough: DIPOLE or BEND to simulate combined function
2423 dipoles, and DRIFT to simulate straight section. A third one CAVITE, is required
2424 for acceleration. Particle monitoring requires keywords introduced in the previous
2425 Chapters, including FAISCEAU, FAISTORE, possibly PICKUPS, and some others.
2426 Spin motion computation and monitoring resort to SPNTRK, SPNPRT, FAISTORE.
2427 Optics matching and optimization use FIT[2]. SYSTEM again is used to shorten the
2428 input data files.

2429 **Notations used in the Text**

| | |
|---------------------------------------|---|
| $B; \mathbf{B}, B_{x,y,s}$ | field value; field vector, its components in the moving frame |
| $B\rho = p/q; B\rho_0$ | particle rigidity; reference rigidity |
| $C; C_0$ | orbit length, $C = 2\pi R + \left[\begin{array}{l} \text{straight} \\ \text{sections} \end{array} \right]$; reference, $C_0 = C(p = p_0)$ |
| E | particle energy |
| EFB | Effective Field Boundary |
| $f_{\text{rev}}, f_{\text{rf}}$ | revolution and accelerating voltage frequencies |
| h | RF harmonic number, $h = f_{\text{rf}}/f_{\text{rev}}$ |
| $m; m_0; M$ | mass, $m = \gamma m_0$; rest mass; in units of MeV/c ² |
| $n = \frac{\rho}{B} \frac{dB}{d\rho}$ | focusing index |
| $\mathbf{p}; p; p_0$ | momentum vector; its modulus; reference |
| P_i, P_f | polarization, initial, final |
| q | particle charge |
| r, R | orbital radius ; average radius, $R = C/2\pi$ |
| s | path variable |
| v | particle velocity |
| $V(t); \hat{V}$ | oscillating voltage; its peak value |
| 2430 x, x', y, y' | horizontal and vertical coordinates in the moving frame |
| α | momentum compaction, or trajectory deviation |
| $\beta = v/c; \beta_0; \beta_s$ | normalized particle velocity; reference; synchronous |
| β_u | betatron functions ($u : x, y, Y, Z$) |
| $\gamma = E/m_0$ | Lorentz relativistic factor |
| δp | momentum offset or Dirac distribution |
| Δp | momentum offset |
| ε | wedge angle |
| ε_u | Courant-Snyder invariant ($u : x, r, y, l, Y, Z, s$, etc.) |
| ε_R | strength of a depolarizing resonance |
| μ_u | betatron phase advance, $\mu_u = \int_{\text{period}} ds/\beta_u(s)$ ($u : x, y, Y, Z$) |
| ν_u | wave number or “tune”, radial, vertical, synchrotron ($u : x, y, Y, Z, l$) |
| ρ, ρ_0 | curvature radius; reference |
| σ | beam matrix |
| $\phi; \phi_s$ | particle phase at voltage gap; synchronous phase |
| ϕ_u | betatron phase advance, $\phi_u = \int ds/\beta_u$ ($u : x, y, Y, or Z$) |
| φ | spin angle to the vertical axis |

2431 **Introduction**

2432 The synchrotron is an outcome of the mid-1940s longitudinal phase focusing syn-
 2433 chronous acceleration concept [1, 2]. In its early version, transverse beam stability
 2434 in the synchrotron during the thousands of turns that the acceleration lasts was based

2435 on the technique known at the time: weak focusing, as in the cyclotron and in the be-
 2436 tatron. An existing betatron was used to first demonstrate phase-stable synchronous
 2437 acceleration with slow variation of the magnetic field, on a fixed orbit, in 1946 [3],
 2438 - closely following the demonstration of the principle of phase focusing using a
 2439 fixed-field cyclotron [4].

2440 Phase focusing states that stability of the longitudinal motion, longitudinal focus-
 2441 ing, is obtained if particles in a bunch, which have a natural energy spread, arrive
 2442 at the accelerating gap in the vicinity of a proper phase of the oscillating voltage,
 2443 the synchronous phase; if this condition is fulfilled the bunch stays together, in the
 2444 vicinity of the latter, during acceleration. Synchrotrons operate in general in a non-
 2445 isochronous regime: the revolution period changes with energy; as a consequence,
 2446 in order to maintain an accelerated bunch on the synchronous phase, the RF voltage
 2447 frequency, which satisfies $f_{\text{rf}} = h f_{\text{rev}}$, has to change continuously from injection to
 2448 top energy. The reference orbit in a synchrotron is maintained at constant radius by
 2449 ramping the guiding field in the main dipoles in synchronism with the acceleration,
 2450 as in the betatron [5].

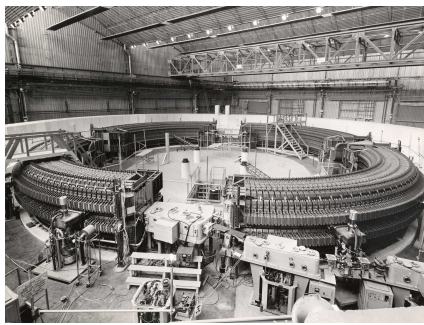


Fig. 9.1 Saturne I at Saclay [6], a 3 GeV, 4-period, 68.9 m circumference, weak focusing synchrotron, constructed in 1956-58. The injection line can be seen in the foreground, injection is from a 3.6 MeV Van de Graaff (not visible)

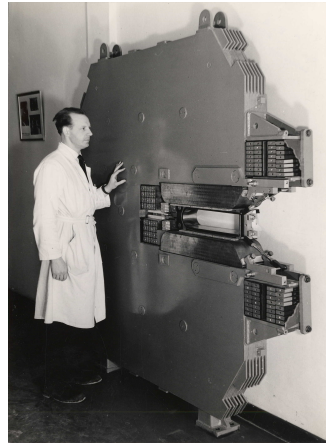


Fig. 9.2 A slice of Saturne I dipole [7]. The slight gap tapering is hardly visible (increasing outward), it determines the weak index condition $0 < n < 1$

2451 The synchrotron concept allowed the highest energy reach by particle accelerators
 2452 at the time, it led to the construction of a series of proton rings with increasing
 2453 energy [8]: 1 GeV at Birmingham (1953), 3.3 GeV at the Cosmotron (Brookhaven
 2454 National Laboratory, 1953-1969), 6.2 GeV at the Bevatron (Berkeley, 1954-1993),
 2455 10 GeV at the Synchro-Phasotron (JINR, Dubna, 1957-2003), and a few additional
 2456 ones in the late 1950s well into the era of the concept which would essentially
 2457 dethrone the weak focusing method and its quite bulky rings of magnets which were

2458 a practical limit to further increase in energy¹: the strong focusing synchrotron (the
 2459 object of Chapter 10). The general layout of these first weak focusing synchrotrons
 2460 included straight sections (often 4, Fig. 9.1), which allowed insertion of injection
 2461 (Fig. 9.1) and extraction systems, accelerating cavities, orbit correction and beam
 2462 monitoring equipment.

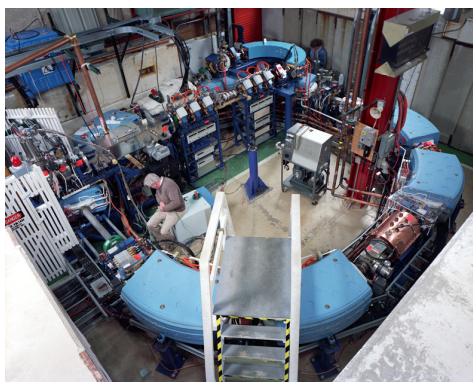


Fig. 9.3 Left: Loma Linda University medical synchrotron, during commissioning in 1989 at the Fermilab National Laboratory where it was designed and constructed [9]

2463 The next decades following the invention of the synchrotron saw applications in
 2464 many fields of science including fixed-target nuclear physics for particle discovery,
 2465 material science, medicine, industry. Its technological simplicity still makes it an
 2466 appropriate technology today in low energy beam application when relatively low
 2467 current is not a concern, as in the hadrontherapy application (Fig. 9.3) [10, 11]: it
 2468 essentially requires a single type of a simple dipole magnet, an accelerating gap, some
 2469 command-control instrumentation, whereas it procures greater beam manipulation
 2470 flexibilities compared to (synchro-)cyclotrons.

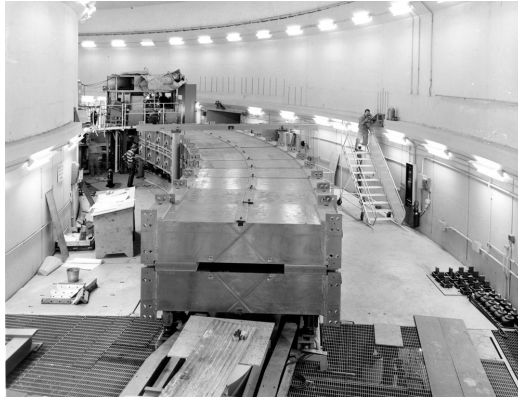
2471 *Polarized beams*

2472 The availability of polarized proton sources allowed the acceleration of polarized
 2473 beams to high energy. The possibility was considered from the early times at Argonne
 2474 ZGS (Zero-Gradient Synchrotron), a 12 GeV weak focusing synchrotron operated
 2475 over 1964-1979 [12] (Fig. 9.4). Up to 70% polarization transmission through the syn-
 2476 chrotron was achieved, for the first time in a synchrotron² and reaching multi-GeV
 2477 energy in 1973, up to 17.5 GeV/c with *appreciable polarizations* [13]. Polariza-
 2478 tion preservation techniques included harmonic orbit correction and fast betatron
 2479 tune jump at strongest depolarizing resonances [14] (Fig. 9.16). Experiments were
 2480 performed to assess the possibility of polarization transmission in strong focusing

¹ The story has it that it is possible to ride a bicycle in the vacuum chamber of Dubna's Synchro-Phasotron.

² Polarized beam had been accelerated in cyclotrons, at earlier times.

Fig. 9.4 The ZGS at Argonne during construction. A 12 GeV, 8-dipole, 4-period, 172 m circumference, wedge focusing synchrotron. The two persons inside and outside the ring, in the background, give an idea of the size of the magnets



2481 synchrotrons, and polarization lifetime in colliders [15]. Acceleration of polarized
2482 deuteron was achieved in the late 1970s, when sources were made available [16].

2483 9.1 Basic Concepts and Formulae

2484 The synchrotron is based on two key principles. On the one hand, a slowly varying
2485 magnetic field to maintain a constant orbit during acceleration,

$$B(t) \times \rho = p(t)/q, \quad \rho = \text{constant}, \quad (9.1)$$

2486 with $p(t)$ the particle momentum and ρ the bending radius in the dipoles. On the other
2487 hand, on synchronous acceleration for longitudinal phase stability. In a regime where
2488 the velocity change with energy cannot be ignored (non-ultrarelativistic particles),
2489 the latter requires a modulation of the accelerating voltage frequency so to satisfy

$$f_{rf}(t) = h f_{rev}(t) \quad (9.2)$$

2490 Synchronism between accelerating voltage oscillation and the revolution motion
2491 keeps the bunch on the synchronous phase at traversal of the accelerating gaps.
2492 Synchronous acceleration is technologically simpler in the case of electrons, as
2493 frequency modulation is unnecessary beyond a few MeV; for instance, from $v/c =$
2494 0.9987 at 10 MeV to $v/c \rightarrow 1$ the relative change in revolution frequency amounts
2495 to $\delta f_{rev}/f_{rev} = \delta\beta/\beta < 0.0013$.

2496 These are two major evolutions compared to the cyclotron, where, instead, the
2497 magnetic field is fixed - the reference orbit spirals out, and, by virtue of the isochro-
2498 nism of the orbits, the oscillating voltage frequency is fixed as well.

2499 A fixed orbit reduces the radial extent of individual guiding magnets, allowing a
2500 ring structure comprised of a circular string of dipoles. For the sake of comparison:
2501 a synchrocyclotron instead uses a single, massive dipole; increased energy requires

2502 increased radial extent of the magnet to allow for the greater bending field integral
 2503 (*i.e.*, $\oint B dl = 2\pi R_{max} \hat{B} = p_{max}/q$), thus a volume of iron increasing more than
 2504 quadratically with bunch rigidity.

2505 One or the other of the weak index ($-1 < k < 0$, Sect. 4.2.2) and/or wedge
 2506 focusing (Sect. 18.3.1) are used in weak focusing synchrotrons. Transverse stability
 2507 was based on the latter at Argonne ZGS (Zero-Gradient Synchrotron: the main
 2508 magnet had no field index); ZGS accelerated polarized proton beams, weak focusing
 2509 resulted in weak depolarizing resonances, an advantage in that matter [15].

2510 Due to the necessary ramping of the field, and of the RF frequency to follow,
 2511 in order to maintain a constant orbit, the synchrotron is a pulsed accelerator, the
 2512 acceleration is cycled, from injection to top energy, repeatedly. The repetition rate
 2513 of the acceleration cycle depends on the type of power supply. If the ramping uses a
 2514 constant electromotive force ($E=V+ZI$ is constant), then

$$B(t) \propto (1 - e^{-\frac{t}{\tau}}) = 1 - \left[1 - \left(\frac{t}{\tau}\right) + \left(\frac{t}{\tau}\right)^2 - \dots \right] \approx \frac{t}{\tau} \quad (9.3)$$

2515 essentially linear; $\dot{B} = dB/dt$ does not exceed a few Tesla/second: the repetition rate
 2516 of the acceleration cycle is of the order of a Hertz. If instead the magnet winding
 2517 is part of a resonant circuit then the field oscillates from an injection threshold to a
 2518 maximum value, $B(t) : B_0 \rightarrow B_0 + \hat{B}$, as in the betatron; the repetition rate is up to
 2519 a few tens of Hertz. In both cases anyway B imposes its law and the other quantities
 2520 comprising the acceleration cycle (RF frequency in particular) will follow B(t).

2521 For the sake of comparison: in a synchrocyclotron the field is constant, thus
 2522 acceleration can be cycled as fast as the swing of the voltage frequency allows
 2523 (hundreds of Hz are common practice); assume a conservative 10 kVolts per turn,
 2524 thus of the order of 10,000 turns to 100 MeV, with velocity $0.046 < v/c < 0.43$
 2525 from 1 to 100 MeV, proton. Take $v \approx 0.5c$ to make it simple, an orbit circumference
 2526 below 30 meter, thus the acceleration takes of the order of $10^4 \times C/0.5c \approx \text{ms}$ range,
 2527 potentially a repetition rate in kHz range, more than an order of magnitude beyond
 2528 the reach of a rapid-cycling pulsed synchrotron.

2529 9.1.1 Periodic Stability

2530 This section introduces the various components of the transverse focusing and the
 2531 conditions for periodic stability in a weak focusing synchrotron. It builds on material
 2532 introduced in Chap. 4, Classical Cyclotron, and on Ref. [17].

2533 9.1.1.1 Closed orbit

2534 The concept is found in the betatron, which accelerates particles on a constant orbit
 2535 (Chap. 7). The closed orbit is fixed, and maintained during acceleration by ensuring

2536 that the relationship Eq. 9.1 is satisfied. In a perfect ring, the closed orbit is along an
 2537 arc in the bending magnets and straight along the drifts, Fig. 9.5.

2538 Particle motion is defined in a moving frame (O;s,x,y) whose origin coincides
 2539 with the location of an ideal particle following the reference orbit. The moving frame
 2540 s axis is tangent to the reference orbit, its transverse horizontal axis x is normal to
 2541 the s axis, its vertical axis y is normal to the (s,x) plane (Fig. 4.8, Sect. 4.2.2).

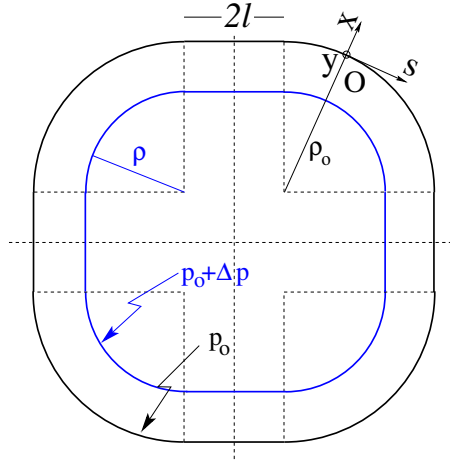


Fig. 9.5 A $2\pi/4$ axially symmetric structure with four drift spaces. Orbit length on reference momentum p_0 is $C = 2\pi\rho_0 + 8l$. (O;s,x,y) is the moving frame, along the reference orbit. The orbit for momentum $p = p_0 + \Delta p$ ($\Delta p < 0$, here) is at constant distance $\Delta x = \frac{\rho_0}{1-n} \frac{\Delta p}{p_0} = \frac{R}{(1+k)(1-n)} \frac{\Delta p}{p_0}$ from the reference orbit

2542 **9.1.1.2 Transverse Focusing**

2543 Radial motion stability around a reference closed orbit in an axially symmetric dipole
 2544 field requires a field index (Sect. 4.2.2),

$$n = -\frac{\rho_0}{B_0} \left. \frac{\partial B_y}{\partial x} \right|_{x=0, y=0} \tag{9.4}$$

2545 a quantity evaluated on the reference arc in the dipoles, satisfying the weak focusing
 2546 condition (Eq. 4.11 with $n = -k$)

$$0 < n < 1 \tag{9.5}$$

2547 This condition can be obtained with a tapered gap (as in Saturne dipoles, Fig. 9.2)
 2548 causing the magnetic field to decrease slowly with radius, so resulting in both axial
 2549 and radial focusing (Figs. 9.6, 9.7). Note the sign convention here, the cyclotron uses
 2550 the opposite sign (Eq. 4.10). This condition holds regardless of the presence of drifts
 2551 or not. Adding drift spaces between the dipoles, the reference orbit is comprised of
 2552 arcs of radius ρ_0 in the magnets, and straight segments along the drift spaces that
 2553 connect these arcs. This requires defining two radii, namely,

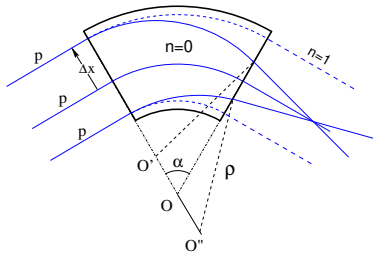


Fig. 9.6 Geometrical focusing: in a sector dipole with focusing index $n = 0$, parallel incoming rays of equal momenta experience the same curvature radius ρ , their trajectories converge as outer trajectories have a longer path in the field, inner ones shorter. An index value $n=1$ cancels that effect: parallel incoming rays exit parallel

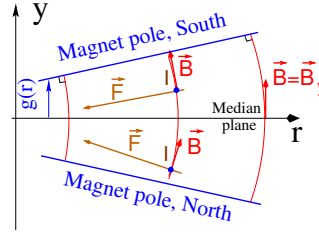


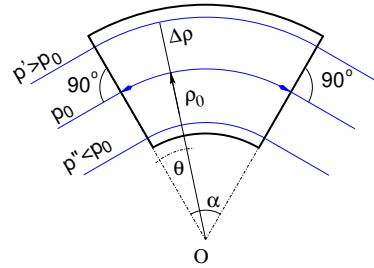
Fig. 9.7 Axial motion stability requires proper shaping of field lines: B_y has to decrease with radius. The Laplace force pulls a positive charge with velocity pointing out of the page, at I, toward the median plane. Increasing the field gradient (n closer to 1, gap opening up faster) increases the focusing

- 2554 (i) the magnet curvature radius ρ_0 ,
- 2555 (ii) an average radius $R = C/2\pi = \rho_0 + Nl/\pi$ (with C the length of the reference
- 2556 closed orbit and $2l$ the drift length) (Fig. 9.5) which also writes

$$R = \rho_0(1 + k), \quad k = \frac{Nl}{\pi\rho_0} \quad (9.6)$$

2557 Adding drift spaces decreases the average focusing around the ring.

Fig. 9.8 In a sector dipole with radial index $n \neq 0$, closed orbits follow arcs of constant field. A closed orbit at $p_0 + \Delta p$ follows an arc of radius $\rho_0 + \Delta\rho$, $\Delta\rho = \Delta p / (1 + n)qB_0$



2558 *Geometrical focusing*

2559 The limit $n \rightarrow 1$ of the transverse motion stability domain corresponds to a cancel-
 2560 lation of the geometrical focusing (Fig. 9.6): in a constant field dipole (radial field
 2561 index $n=0$) the longer (respectively shorter) path in the magnetic field for parallel
 2562 trajectories entering the magnet at greater (respectively smaller) radius result in
 2563 convergence. This effect is cancelled, *i.e.*, the deviation is the same whatever the

2564 entrance radius, if the curvature center is made independent of the entrance radius:
 2565 $OO' = 0, O''O = 0$. This occurs if trajectories at an outer (inner) radius experience a
 2566 smaller (greater) field such as to satisfy $BL = B\rho\alpha = C^{st}$. Differentiating $B\rho = C^{st}$
 2567 gives $\frac{\Delta B}{B} + \frac{\Delta\rho}{\rho} = 0$, with $\Delta\rho = \Delta x$, so yielding $n = -\frac{\rho_0}{B_0} \frac{\Delta B}{\Delta x} = 1$. The focal distance
 2568 associated with the curvature is (Eq. 4.12 with $R = \rho_0$) $f = \frac{\rho_0^2}{L}$. Optical drawbacks
 2569 of the weak focusing method include the weakness of the focusing and the absence
 2570 of independent radial and axial focusing.

2571 *Wedge Focusing*

2572 Entrance and exit wedge angles may be used to ensure transverse focusing, Fig. 9.9:
 2573 opening the magnetic sector increases the horizontal focusing (and decreases the
 2574 vertical focusing); closing the magnetic sector has the reverse effect (see Sect. 18.3.1).

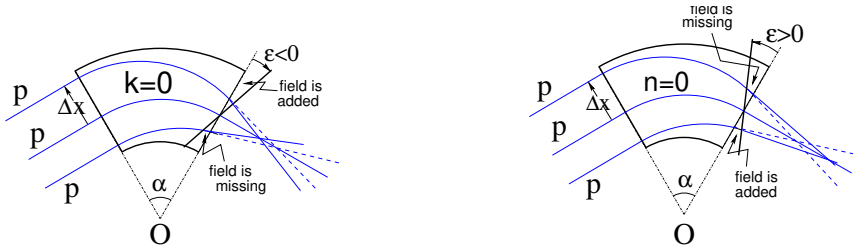


Fig. 9.9 Left: a focusing wedge ($\varepsilon < 0$); opening the sector increases horizontal focusing and decreases vertical focusing. Right: a defocusing wedge ($\varepsilon > 0$), closing the sector, has the reverse effect. This is the origin of the focusing in the ZGS zero-gradient dipoles

2575 In a point transform approximation, at the wedge the trajectory undergoes a local
 2576 deviation proportional to the distance to the optical axis, amounting to

$$\Delta x' = \frac{\tan \varepsilon}{\rho_0} \Delta x, \quad \Delta y' = -\frac{\tan(\varepsilon - \psi)}{\rho_0} \Delta y \quad (9.7)$$

2577 The ψ angle component is a correction for the fringe field extent (Eq. 18.21); the
 2578 effect of the latter, of the first order on the vertical focusing, is of second order
 2579 horizontally.

2580 Profiling the magnet gap in order to adjust the focal distance complicates the
 2581 magnet; a parallel gap, $n = 0$, makes it simpler, for that reason edge focusing may
 2582 be preferred. Wedge vertical focusing in the ZGS ($\varepsilon > 0$) was at the expense of
 2583 horizontal geometrical focusing (Fig. 9.6). This was an advantage though, for the
 2584 acceleration of polarized beams, as radial field components (which are responsible for
 2585 depolarization) were only met at the EFBs of the eight main dipoles, and weak [13].
 2586 Preserving beam polarization at high energy required tight control of the tunes, this

2587 was achieved by pole face windings added at the ends of the dipoles [18, 19], pulsed
2588 to control the amplitude detuning, resulting in a control of the tunes at 0.01 level.

2589 9.1.1.3 Periodic stability, betatron motion

2590 The first order differential equations of motion in the moving frame (Fig. 9.5) derive
2591 from the Lorentz equation

$$\frac{d\mathbf{m}\mathbf{v}}{dt} = q\mathbf{v} \times \mathbf{B} \Rightarrow m \frac{d}{dt} \begin{Bmatrix} \frac{ds}{dt} \mathbf{s} \\ \frac{dx}{dt} \mathbf{x} \\ \frac{dy}{dt} \mathbf{y} \end{Bmatrix} = q \begin{Bmatrix} \left(\frac{dx}{dt} B_y - \frac{dy}{dt} B_x \right) \mathbf{s} \\ -\frac{ds}{dt} B_y \mathbf{x} \\ \frac{ds}{dt} B_x \mathbf{y} \end{Bmatrix} \quad (9.8)$$

2592 Motion in a weak index dipole field is solved in Sect. 4.2.2, Classical Cyclotron: in
2593 the latter substitute ρ to R , $n = -\frac{\rho_0}{B_0} \frac{\partial B_y}{\partial x}$ to $-k$, evaluated on the reference orbit.
2594 Taylor expansions of the transverse field components in the moving frame (Eq. 4.6)
2595 lead to

$$\begin{aligned} B_y(\rho)|_{y=0} &= B_0(1 - n \frac{x}{\rho_0}) + \mathcal{O}(x^2) \\ B_x(0+y) &= -n \frac{B_0}{\rho_0} y + \mathcal{O}(y^3) \end{aligned} \quad (9.9)$$

2596 Assume transverse stability: $0 < n < 1$; in the approximation $ds \approx vdt$ (Eq. 4.13)
2597 Eqs. 9.8, 9.9 lead to the differential equations of motion

$$\frac{d^2x}{ds^2} + \frac{1-n}{\rho_0^2} x = 0, \quad \frac{d^2y}{ds^2} + \frac{n}{\rho_0^2} y = 0 \quad (9.10)$$

2598 It results that, in an S-periodic structure comprised of gradient dipoles, wedges
2599 and drift spaces, the differential equation of motion takes the general form of Hill's
2600 equation, a second order differential equation with periodic coefficient, namely (with
2601 u standing for x or y),

$$\begin{cases} \frac{d^2u}{ds^2} + K_u(s)u = 0 \\ K_u(s+S) = K_u(s) \end{cases} \quad \text{with} \quad \begin{cases} \text{in dipoles : } \begin{cases} K_x = \frac{1-n}{\rho_0^2} \\ K_y = \frac{n}{\rho_0^2} \end{cases} \\ \text{at a wedge at } s = s_0 : K_x = \frac{\pm \tan \varepsilon}{\rho_0} \delta(s - s_0) \\ \text{in drift spaces : } \frac{1}{\rho_0} = 0, K_x = K_y = 0 \end{cases} \quad (9.11)$$

2602 $K_u(s)$ is S-periodic, $S = 2\pi R/N$ ($S = C/4$ for instance in a 4-periodic ring,
2603 Figs. 9.1, 9.5).

2604 The solution of Eqs. 9.11 is not as straightforward as in the cyclotron where K_u
2605 is constant around the ring (Eq. 4.14), which results in a sinusoidal motion (Eq. 4.16)
2606 - the latter is on the other hand a reasonable approximation, see below, *Weak focusing*
2607 *approximation*. G. Floquet has established [20] that the two independent solutions
2608 of Hill's second order differential equation have the form [17]

$$\left\{ \begin{array}{l} u_1(s) = \sqrt{\beta_u(s)} e^{i \int_0^s \frac{ds}{\beta_u(s)}} \\ du_1(s)/ds = \frac{i - \alpha_u(s)}{\beta_u(s)} u_1(s) \end{array} \right. \quad \text{and} \quad \left\{ \begin{array}{l} u_2(s) = u_1^*(s) \\ du_2(s)/ds = du_1^*(s)/ds \end{array} \right. \quad (9.12)$$

2609 wherein $\beta_u(s)$ and $\alpha_u(s) = -\beta'_u(s)/2$ are S-periodic functions, from what it results
2610 that

$$u_{\frac{1}{2}}(s+S) = u_{\frac{1}{2}}(s) e^{\pm i \mu_u} \quad (9.13)$$

2611 wherein

$$\mu_u = \int_{s_0}^s \frac{ds}{\beta_u(s)} \quad (9.14)$$

2612 is the betatron phase advance at s , from the origin s_0 . A real solution of Hill's
2613 equation is the linear combination $A u_1(s) + A^* u_2^*(s)$. With $A = \frac{1}{2} \sqrt{\varepsilon_u/\pi} e^{i\phi}$
2614 following conventional notations, with ϕ the phase at the origin, the general solution
2615 of Eq. 9.11 writes

$$\left\{ \begin{array}{l} u(s) = \sqrt{\beta_u(s) \varepsilon_u/\pi} \cos\left(\int_{s_0}^s \frac{ds}{\beta_u} + \phi\right) \\ u'(s) = -\sqrt{\frac{\varepsilon_u/\pi}{\beta_u(s)}} \sin\left(\int_{s_0}^s \frac{ds}{\beta_u} + \phi\right) + \alpha_u(s) \cos\left(\int_{s_0}^s \frac{ds}{\beta_u} + \phi\right) \end{array} \right. \quad (9.15)$$

2616 An invariant of the motion, known as the Courant-Snyder invariant, is

$$\frac{1}{\beta_u(s)} \left[u^2 + (\alpha_u(s)u + \beta_u(s)u')^2 \right] = \frac{\varepsilon_u}{\pi} \quad (9.16)$$

2617 At a given azimuth s of the periodic structure the observed turn-by-turn motion
2618 lies on that ellipse (Fig. 9.10). The form and inclination of the ellipse depend on
2619 the observation azimuth s via the respective local values of $\alpha_u(s)$ and $\beta_u(s)$, but
2620 its surface ε_u is invariant. Motion along the ellipse is clockwise, as can be figured
2621 from Eq. 9.15 considering an observation azimuth s where the ellipse is upright,
2622 $\alpha_u(s) = 0$. In an N-periodic ring, the phase advance over a turn (from one location
2623 to the next on the ellipse in Fig. 9.10) is

$$\int_{s_0}^{s_0+NS} \frac{ds}{\beta_u(s)} = N \int_{\text{period}} \frac{ds}{\beta_u(s)} = N \mu_u \quad (9.17)$$

2624 *Weak focusing approximation*

2625 In a cylindrically symmetric structure a sinusoidal motion is the exact solution of the
2626 first order differential equations of motion (Eqs. 4.15, 4.16, Classical Cyclotron Chap-
2627 ter), the coefficients $K_x = (1-n)/R_0^2$ and $K_y = n/R_0^2$ are constant (s-independent).
2628 Adding drift spaces results in Hill's differential equation with periodic coefficient
2629 $K(s+S) = K(s)$ (Eq. 9.11), and in a pseudo harmonic solution (Eq. 9.15). Due to the

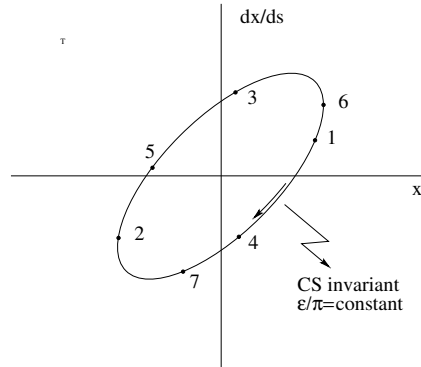


Fig. 9.10 Courant-Snyder invariant and turn-by-turn harmonic motion along the invariant, observed at some azimuth s . The form of the ellipse depends on the observation azimuth s but its surface ε_u is invariant

2630 weak focusing the beam envelope is only weakly modulated (see below), thus so is
 2631 $\beta_u(s)$. In a practical manner, the modulation of $\beta_u(s)$ does not exceed a few percent,
 2632 this justifies introducing the average value $\overline{\beta_u}$ to approximate the phase advance by

$$\int_0^s \frac{ds}{\beta_u(s)} \approx \frac{s}{\overline{\beta_u}} = \nu_u \frac{s}{R} \quad (9.18)$$

2633 The right equality is obtained by applying this approximation to the phase advance
 2634 per period, namely (Eq. 9.14) $\mu_u = \int_{s_0}^{s_0+S} \frac{ds}{\beta_u(s)} \approx S/\overline{\beta_u}$, and introducing the wave
 2635 number of the N-period optical structure $\nu_u = \frac{N\mu_u}{2\pi} = \frac{\text{phase advance over a turn}}{2\pi}$ so that

$$\overline{\beta_u} = \frac{R}{\nu_u} \quad (9.19)$$

2636 the wavelength of the betatron oscillation around the ring. With $k \ll 1$ and using
 2637 Eq. 9.23,

$$\overline{\beta_x} = \frac{\rho_0(1+k/2)}{\sqrt{1-n}}, \quad \overline{\beta_y} = \frac{\rho_0(1+k/2)}{\sqrt{n}} \quad (9.20)$$

2638 Substituting $\nu_u \frac{s}{R}$ to $\int \frac{ds}{\beta_u(s)}$ in Eq. 9.15 yields the approximate solution

$$\begin{cases} u(s) \approx \sqrt{\beta_u(s)\varepsilon_u/\pi} \cos\left(\nu_u \frac{s}{R} + \phi\right) \\ u'(s) \approx -\sqrt{\frac{\varepsilon_u/\pi}{\beta_u(s)}} \sin\left(\nu_u \frac{s}{R} + \phi\right) + \alpha_u(s) \cos\left(\nu_u \frac{s}{R} + \phi\right) \end{cases} \quad (9.21)$$

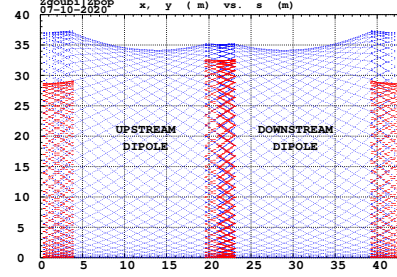
2639 *Beam envelopes*

2640 The beam envelope $\hat{u}(s)$ (with u standing for x or y) is determined by the particle of
 2641 maximum invariant ε_u/π , it is given at all s by

$$\pm \hat{u}(s) = \pm \sqrt{\beta_u(s) \varepsilon_u / \pi} \quad (9.22)$$

As $\beta_u(s)$ is S-periodic, so is the envelope, $\hat{u}(s+S) = \hat{u}(s)$. In a cell with symmetries,

Fig. 9.11 Multi-turn particle excursion along the ZGS 2-dipole 43 m cell. The motion extrema (Eq. 9.22) tangent the envelopes, respectively horizontal (red), and vertical (blue). Envelopes have the symmetry of the cell



2642
 2643 beam envelopes feature the same symmetries, as in Fig. 9.11 for instance: a symmetry
 2644 with respect to the center of the cell; envelop extrema are at azimuth s of $\beta_u(s)$
 2645 extrema, *i.e.* where $d\hat{u}(s)/ds \propto \beta'_u(s) = 0$ or $\alpha_u = 0$ as $\beta'_u = -2\alpha_u$.

2646 *Working point*

2647 The “working point” of the synchrotron is the wave number couple (ν_x, ν_y) at which
 2648 the accelerator is operated, it fully characterizes the focusing. In a structure with
 2649 cylindrical symmetry (such as the Classical Cyclotron) $\nu_x = \sqrt{1-n}$ and $\nu_y = \sqrt{n}$
 2650 (Eq. 4.17) so that $\nu_x^2 + \nu_y^2 = 1$: when the radial field index n is changed the working
 2651 point stays on a circle of radius 1 in the stability diagram (or “tune diagram”,
 2652 Fig. 9.12). If drift spaces are added, from Eqs. 9.19, 9.20, with $1 + \frac{k}{2} \approx \sqrt{R/\rho_0}$
 2653 (Eq. 9.6), it comes

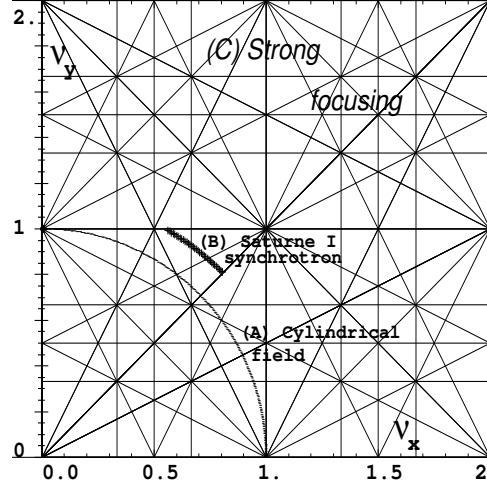
$$\nu_x = \sqrt{(1-n) \frac{R}{\rho_0}}, \quad \nu_y = \sqrt{n \frac{R}{\rho_0}}, \quad \nu_x^2 + \nu_y^2 = \frac{R}{\rho_0} \quad (9.23)$$

thus the working point is located on the circle of radius $\sqrt{R/\rho_0} > 1$ (Fig. 9.12).
 Tunes can not exceed the limits

$$0 < \nu_{x,y} < \sqrt{R/\rho_0}$$

2654 Horizontal and vertical focusing are not independent (Eq. 9.11): if ν_x increases then
 2655 ν_y decreases and reciprocally. This is a lack of flexibility which the advent of strong
 2656 focusing will overcome by providing two knobs allowing separate adjustment of the
 2657 tunes.

Fig. 9.12 Location of the working point in the tune diagram, in case of (A) field with revolution symmetry, on a circle of radius 1; (B) sector field with index + drift spaces, on a circle of radius $(\sqrt{R/\rho_0})$. Case (C) is for strong focusing, $(|n| \gg 1)$, ν_x and ν_y are large



2658 Off-momentum orbits; periodic dispersion

2659 In the linear approximation in $\Delta p/p_0$, a momentum offset $\Delta p = p - p_0$ changes
 2660 mv to $mv(1 + \Delta p/p_0)$ in Eq. 9.8; this changes the horizontal equation of motion
 2661 (Eq. 9.10) to

$$\frac{d^2x}{ds^2} + K_x x = \frac{1}{\rho_0} \frac{\Delta p}{p_0}, \quad \text{or} \quad \frac{d^2x}{ds^2} + K_x \left(x - \frac{1}{\rho_0 K_x} \frac{\Delta p}{p_0} \right) = 0 \quad (9.24)$$

2662 A change of variable $x - \frac{1}{K_x \rho_0} \frac{\Delta p}{p_0} \rightarrow x$ (with $1/\rho_0 K_x = \rho_0/(1-n)$) restores the
 2663 unpertrurbed equation of motion; thus orbits of different momenta $p = p_0 + \Delta p$ are
 2664 distant

$$\Delta x = \frac{\rho_0}{1-n} \frac{\Delta p}{p_0} \quad (9.25)$$

2665 from the reference orbit (Fig. 9.8). Introduce the geometrical radius $R = (1+k)\rho_0$
 2666 (Eq. 9.6) to account for the added drifts; this yields the dispersion function

$$D_x = \frac{\Delta x}{\Delta p/p_0} \equiv \frac{\Delta R}{\Delta p/p_0} = \frac{R}{(1-n)(1+k)} = \frac{\rho_0}{1-n}, \quad \text{constant} \quad (9.26)$$

2667 D_x is the chromatic dispersion of the orbits, an s -independent quantity: in a structure
 2668 with axial symmetry, comprising drift sections (Fig. 9.5) or not (classical and AVF
 2669 cyclotrons for instance), the ratio $\frac{\Delta x}{\rho_0 \Delta p/p_0}$ is independent of the azimuth s , the
 2670 distance of a chromatic orbit to the reference orbit is constant around the ring.

2671 Given that $n < 1$,

- 2672 - higher momentum orbits, $p > p_0$, have a greater radius,
- 2673 - lower momentum orbits, $p < p_0$, have a smaller radius.

2674 The horizontal harmonic motion of an off-momentum particle thus writes

$$x(s) = \sqrt{\beta_u(s)\varepsilon_u/\pi} \cos\left(\nu_u \frac{s}{R} + \phi\right) + \frac{\rho_0}{1-n} \frac{\Delta p}{p_0} \quad (9.27)$$

2675 *Chromatic orbit length*

2676 In an axially symmetric structure the difference in closed orbit length $\Delta C = 2\pi\Delta R$
 2677 resulting from the difference in momentum arises in the dipoles, as all orbits are
 2678 parallel in the drifts (Fig. 9.5). Hence, from Eq. 9.26, the relative closed orbit
 2679 lengthening factor, or momentum compaction

$$\alpha = \frac{\Delta C}{C} \bigg/ \frac{\Delta p}{p_0} \equiv \frac{\Delta R}{R} \bigg/ \frac{\Delta p}{p_0} = \frac{1}{(1-n)(1+k)} \approx \frac{1}{\nu_x^2} \quad (9.28)$$

2680 with $k = Nl/\pi\rho_0$ (Eq. 9.6). Note that the relationship $\alpha \approx 1/\nu_x^2$ between momentum
 2681 compaction and horizontal wave number established for a revolution symmetry
 2682 structure (Eq. 4.21) still holds when adding drifts.

2683 9.1.1.4 Longitudinal Motion

2684 In a synchrotron, the field B is varied during acceleration (a function performed
 2685 by the power supply) concurrently with the variation of the bunch momentum p (a
 2686 function performed by the accelerating cavity) in such a way that at any time

$$\Delta W = F \times 2\pi R = 2\pi q R \rho \dot{B} B(t) \rho = p(t)/q \quad (9.29)$$

so that the beam is maintained on the design orbit. Given the energies involved, the
 magnet supply imposes its law and the cavity follows $B(t)$ (Fig. 9.13), the best it
 can. The accelerating voltage $\hat{V}(t) = \sin \omega_{\text{rf}} t$ is maintained in synchronism with the
 revolution motion, its angular frequency satisfying

$$\omega_{\text{rf}} = h\omega_{\text{rev}} = h \frac{c}{R} \frac{B(t)}{\sqrt{\left(\frac{m_0}{q\rho}\right)^2 + B^2(t)}}$$

2687 *Energy gain*

2688 The variation of the particle energy over a turn amounts to the work of the force
 2689 $F = dp/dt$ on the charge at the cavity, namely

$$\Delta W = F \times 2\pi R = 2\pi q R \rho \dot{B} \quad (9.30)$$

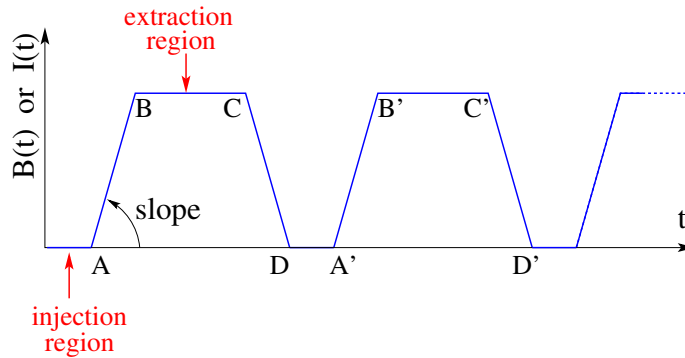


Fig. 9.13 Cycling $B(t)$ in a pulsed synchrotron. Ignoring saturation, $B(t)$ is proportional to the magnet power supply current $I(t)$. Beam injection occurs at low field, in the region of A, extraction occurs at top energy, on the high field plateau. (AB): field ramp up (acceleration); (BC): flat top; (CD): field ramp down; (DA'): thermal relaxation. (AA'): repetition period; $(1/AA')$: repetition rate; *slope*: ramp velocity $\dot{B} = dB/dt$ (Tesla/s).

Over most of the acceleration cycle in a slow-cycling synchrotron \dot{B} is usually constant (Eq. 9.3), thus so is ΔW . At Saturne I for instance (the object of Exercise 9.1, parameters in Tab. 9.1)

$$\frac{\Delta W}{q} = 2\pi R\rho\dot{B} = 68.9 \times 8.42 \times 1.8 = 1044 \text{ volts}$$

The field ramp lasts

$$\Delta t = (B_{\max} - B_{\min})/\dot{B} \approx B_{\max}/\dot{B} = 0.8 \text{ s}$$

The number of turns to the top energy ($W_{\max} \approx 3 \text{ GeV}$) is

$$N = \frac{W_{\max}}{\Delta W} = \frac{3 \cdot 10^9 \text{ eV}}{1044 \text{ eV/turn}} \approx 3 \cdot 10^6 \text{ turns}$$

The dependence of particle mass on field writes

$$m(t) = \gamma(t)m_0 = \frac{q\rho}{c} \sqrt{\left(\frac{m_0}{qc\rho}\right)^2 + B(t)^2}$$

2690 *Adiabatic damping of the betatron oscillations*

The focusing index (Eq. 9.4) does not change during acceleration, thus the tunes ν_x and ν_y do not change either. As a result of the longitudinal acceleration at the cavity though, the longitudinal energy of the particles is modified. This results in a decrease of the amplitude of betatron oscillations (an increase if the cavity is decelerating).

The mechanism is sketched in Fig. 9.14: the slope, respectively before and after (index 2) the cavity is

$$\frac{dx}{ds} = \frac{m \frac{dx}{dt}}{m \frac{ds}{dt}} = \frac{p_x}{p_s}, \quad \frac{dx}{ds} \Big|_2 = \frac{m \frac{dx}{dt}}{m \frac{ds}{dt}} \Big|_2 = \frac{p_{x,2}}{p_{s,2}}$$

Particle mass and velocity are modified at the traversal of the cavity but, as the

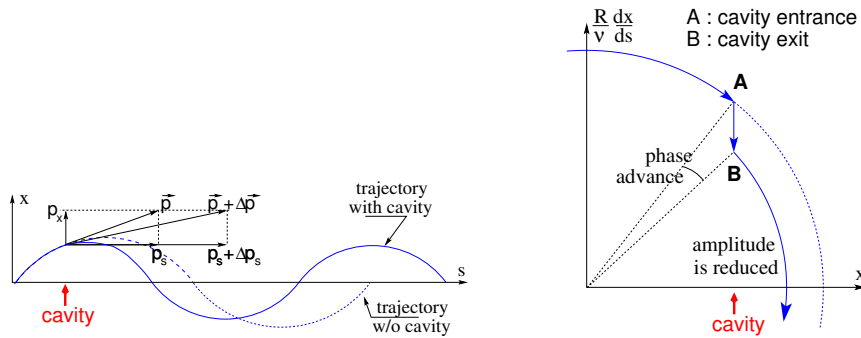


Fig. 9.14 Adiabatic damping of betatron oscillations, here from $x' = p_x/p_s$ before the cavity, to $x'_2 = p_x/(p_s + \Delta p_s)$ after the cavity. In the horizontal phase space, to the right, decrease of $\Delta \left(\frac{dx}{ds} \right)$ if $\frac{dx}{ds} > 0$, increase of $\Delta \left(\frac{dx}{ds} \right)$ if $\frac{dx}{ds} < 0$

force is longitudinal, $dp_x/dt = 0$ thus $p'_x = p_x$, the increase in momentum is purely longitudinal, $p'_s = p_s + \Delta p$. Thus

$$\frac{dx}{ds} \Big|_2 = \frac{p_x}{p_s + \Delta p} \approx \frac{p_x}{p_s} \left(1 - \frac{\Delta p}{p_s} \right)$$

and as a consequence the slope dx/ds varies across the cavity,

$$\Delta \left(\frac{dx}{ds} \right) = \frac{dx}{ds} \Big|_2 - \frac{dx}{ds} = - \frac{dx}{ds} \frac{\Delta p_s}{p_s}$$

2691 The variation of the slope is proportional to the slope, with opposite sign if $\Delta p/p > 0$
 2692 (acceleration) thus a decrease of the slope. This variation has two consequences on
 2693 the betatron oscillation (Fig. 9.14):

- 2694 - a change of the betatron phase,
- 2695 - a modification of the betatron amplitude.

2696 *Coordinate transport*

2697 at the cavity writes $\begin{cases} x_2 = x \\ x_2' \approx \frac{p_x}{p_s} (1 - \frac{dp}{p}) = x'(1 - \frac{dp}{p}) \end{cases}$. In matrix form, $\begin{pmatrix} x_2 \\ x_2' \end{pmatrix} =$
 2698 $[C] \begin{pmatrix} x \\ x' \end{pmatrix}$ with

$$[C] = \begin{bmatrix} 1 & 0 \\ 0 & 1 - \frac{dp}{p} \end{bmatrix} \quad (9.31)$$

2699 and $\det[C] = 1 - \frac{dp}{p} \neq 1$: the system is non-conservative, the surface of the beam
 2700 ellipse in phase space is not conserved. Assume one cavity in the ring and note
 2701 $[T] \times [C]$ the one-turn coordinate transport matrix with origin at entrance of the
 2702 cavity. Its determinant is $\det[T] \times \det[C] = \det[C] = 1 - \frac{dp}{p}$; the variation of
 2703 the transverse ellipse surface satisfies $\varepsilon_u = (1 - \frac{dp}{p_0})\varepsilon_0$ or, with $d\varepsilon_u = \varepsilon_u - \varepsilon_0$,
 2704 $\frac{d\varepsilon_u}{\varepsilon_u} = -\frac{dp}{p_0}$, the solution of which is

$$p \varepsilon_u = \text{constant}, \text{ or } \beta\gamma\varepsilon_u = \text{constant} \quad (9.32)$$

2705 Over N turns the coordinate transport matrix is $[T_N] = ([T][C])^N$, its determinant
 2706 is $(1 - \frac{dp}{p})^N \approx 1 - N\frac{dp}{p}$: the ellipse surface changes by that factor.

2707 *Synchrotron motion; phase stability*

2708 “Synchrotron motion” designates the mechanism of phase stability, or longitudinal
 2709 focusing (Fig. 9.15), that stabilizes the longitudinal motion of a particle in the vicinity
 2710 of a synchronous phase, ϕ_s , in virtue of

2711 (i) the presence of an accelerating cavity with its frequency indexed on the
 2712 revolution time,

2713 (ii) with the bunch centroid positioned either on the rising slope of the oscillating
 2714 voltage (low energy regime), or on the falling slope (high energy regime).

The synchronous (or “ideal”) particle follows the equilibrium trajectory around
 the ring (the reference closed orbit, about which all other particles will undergo a
 betatron oscillation), its velocity satisfies $v(t) = \frac{qB\rho(t)}{m}$; at each turn it reaches the
 accelerating gap when the oscillating voltage is at the synchronous phase ϕ_s , and
 undergoes an energy gain

$$\Delta W = q\hat{V} \sin \phi_s$$

The condition $|\sin \phi_s| < 1$ imposes a lower limit to the cavity voltage for acceleration
 to happen, namely, after Eq. 9.30,

$$\hat{V} > 2\pi R\rho\dot{B}$$

2715 Referring to Fig. 9.15, the synchronous phase can be placed on the left (A A' A''...
 2716 series in the Figure, or on the right (B B' B''... series) of the oscillating voltage crest.

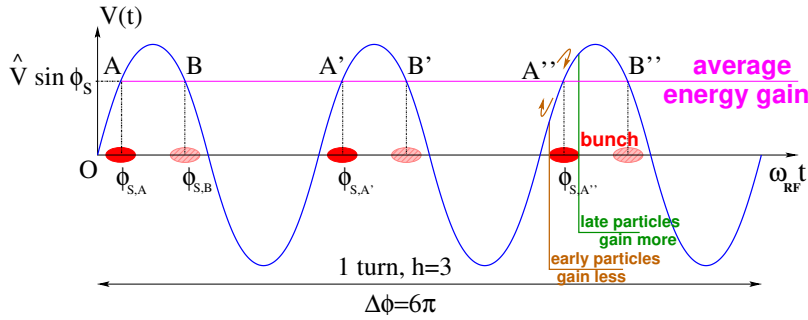


Fig. 9.15 A sketch of the mechanism of phase stability, $h = 3$ in this example. Below transition phase stability occurs for a synchronous phase taken at either one of A, A', A'' arrival times at the gap: a particle with higher energy goes around the ring more rapidly than the synchronous particle; if both are launched together, the former arrives earlier at the voltage gap (at $\phi < \phi_{s,A}$) so experiencing weaker acceleration; at lower energy the particle is slower, it arrives at the gap later, $\phi > \phi_{s,A}$, so experiencing a greater voltage; this results in an overall stable oscillatory motion around the synchronous phase. Beyond transition the stable phase is at either one of B, B', B'' locations: a particle which is less energetic than the synchronous particle arrives earlier, $\phi < \phi_{s,B}$, so experiencing a greater voltage, and inversely, resulting in overall stable synchrotron motion.

2717 One and only one of these two possibilities, and which one depending upon the optical
 2718 lattice and on particle energy, ensures that particles in a bunch remain grouped in
 2719 the vicinity of the synchronous particle. The transition is between two time-of-flight
 2720 regimes: a particle which gains momentum compared to the synchronous particle
 2721 has a greater velocity, while

2722 - in the high bunch energy regime the increase in path length around the ring
 2723 is faster than the increase in velocity (velocity essentially does not even change
 2724 in ultrarelativistic regime), a revolution around the ring takes more time (this is the
 2725 classical cyclotron and synchrocyclotron regime, and as well the high energy electron
 2726 synchrotron regime); consider such a particle, arriving at the accelerating gap late
 2727 ($\phi(t) > \phi_s$), in order for it to be pulled toward bunch center (*i.e.*, take less time
 2728 around the ring) it has to undergo deceleration; this is the B series, above transition;
 2729 - in the low bunch energy regime velocity increase is faster than path length
 2730 increase, thus a revolution around the ring is faster; consider such a particle, arriving
 2731 at the accelerating gap early ($\phi(t) < \phi_s$), in order for it to be pulled toward bunch
 2732 center (*i.e.*, take more time around the ring) it has to be slowed down, it has to
 2733 undergo deceleration; this is the A series, below transition.

2734 *Transition energy*

2735 The transition between the two time-of-flight regimes occurs at $\frac{dT_{\text{rev}}}{T_{\text{rev}}} = 0$. With
 2736 $T = 2\pi/\omega = C/v$, this can be written $\frac{d\omega_{\text{rev}}}{\omega_{\text{rev}}} = -\frac{dT_{\text{rev}}}{T_{\text{rev}}} = \frac{dv}{v} - \frac{dC}{C}$. With $\frac{dv}{v} = \frac{1}{\gamma^2} \frac{dp}{p}$

2737 and momentum compaction $\alpha = \frac{dC}{C} / \frac{dp}{p}$, (Eq. 9.28), this can be written

$$\frac{d\omega_{\text{rev}}}{\omega_{\text{rev}}} = -\frac{dT_{\text{rev}}}{T_{\text{rev}}} = \left(\frac{1}{\gamma^2} - \alpha \right) \frac{dp}{p} = \eta \frac{dp}{p} \quad (9.33)$$

2738 wherein the phase-slip factor has been introduced,

$$\eta = \overbrace{\frac{1}{\gamma^2}}^{\text{kinematics}} - \underbrace{\alpha}_{\text{lattice}} = \frac{1}{\gamma^2} - \frac{1}{\gamma_{\text{tr}}^2} \quad (9.34)$$

2739 The transition γ appears to be a property of the lattice.

2740 In a weak focusing lattice $\gamma_{\text{tr}} = 1/\sqrt{\alpha} \approx v_x$ (Eqs. 4.21, 9.28), thus the phase
2741 stability regime is

$$\begin{aligned} &\text{below transition, i.e. } \phi_s < \pi/2, \quad \text{if } \gamma < v_x \\ &\text{above transition, i.e. } \phi_s > \pi/2, \quad \text{if } \gamma > v_x \end{aligned} \quad (9.35)$$

2742 In a weak focusing synchrotron the horizontal tune $\nu_x = \sqrt{(1-n)R/\rho_0}$ (Eq. 9.23)
2743 may be ≥ 1 , and subsequently $\gamma_{\text{tr}} > 1$ is a possibility. There is no transition-gamma
2744 if $\nu_x < 1$. Acceleration to 3 GeV in Saturne I for instance, from 50 MeV at injection,
2745 and with $\nu_x \approx 0.7$ (Tab. 9.1) did not require transition-gamma crossing³.

2746 9.1.2 Spin Motion, Depolarizing Resonances

2747 The field index is essentially zero in the ZGS, transverse focusing is ensured by
2748 wedge angles at the ends of the height dipoles, which is thus the only location where
2749 non-zero horizontal field components are found. As a consequence depolarizing
2750 resonances are weak: “As we can see from the table, the transition probability [from
2751 spin state $\psi_{1/2}$ to spin state $\psi_{-1/2}$] is reasonably small up to $\gamma = 7.1$ ” [13], i.e.
2752 $G\gamma = 12.73$, $p = 6.6$ GeV/c; the table referred to stipulates a transition probability
2753 $P_{\frac{1}{2}, -\frac{1}{2}} < 0.042$, whereas resonances beyond that energy range feature $P_{\frac{1}{2}, -\frac{1}{2}} > 0.36$.
2754 Beam depolarization up to 6 GeV/c, under the effect of these resonances, is illustrated
2755 in Fig. 9.16.

2756 In a synchrotron using gradient dipoles, particles experience radial fields all along
2757 the latter as they undergo vertical betatron oscillations, as an effect of the radial field
2758 index [13, 21, 22]. However these radial field components are weak, and so is there

³ Transition-gamma crossing, or “gamma jump”, is a common beam manipulation during acceleration in strong focusing synchrotrons, it requires an RF phase jump, the technique is addressed in Chapter 10.

2759 effect on spin motion as long as the particle energy is low enough (an effect of the γ
 2760 factor in the spin precession Eq. 4.29, Chap. 4).

Assuming a defect-free ring, the vertical betatron motion excites “intrinsic” spin resonances, located at

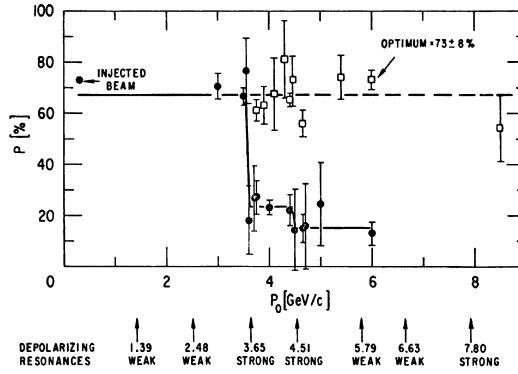
$$G\gamma_R = k P \pm \nu_y$$

with k an integer and P the period of the ring. In the ZGS for instance, $\nu_y \approx 0.8$ (Tab. 9.2), the ring is $P=4$ -periodic, thus $G\gamma_R = 4k \pm 0.8$. Strongest resonances are located at

$$G\gamma_R = mk P \pm \nu_y$$

2761 with m the number of cells per superperiod [23, Sec. 3.II]. In the ZGS, $m=2$ thus
 2762 strongest resonances occur at $G\gamma_R = 2 \times 4k \pm 0.8 = 7.2$ ($p = 3.65$ GeV/c), 8.8 (4.51 GeV/c), 15.2 (7.9 GeV/c), ... (Fig. 9.16).

Fig. 9.16 Depolarizing intrinsic resonance landscape up to 9 GeV/c at the ZGS (solid circles) [24]. Systematic resonances are located at $G\gamma_R = 4 \times \text{integer} \pm \nu_y$, stronger ones at $G\gamma_R = 8 \times \text{integer} \pm \nu_y$. A tune jump was applied to preserve polarization when crossing strong resonances (empty circles)



2763 In the presence of vertical orbit defects, non-zero periodic transverse fields are experienced along the closed orbit, they excite “imperfection” depolarizing resonances, located at

$$G\gamma_R = k$$

with k an integer. In the case of systematic defects the periodicity of the orbit is that of the lattice, P , imperfection resonances are located at $G\gamma_R = kP$. Strongest imperfection resonances are located at [23, Sec. 3.II]

$$G\gamma_R = mk P$$

2764 Crossing a depolarizing resonance of strength ϵ_R causes a loss of polarization
 2765 given by (Froissart-Stora formula [25])

$$\frac{P_f}{P_i} = 2e^{-\frac{\pi}{2} \frac{|\epsilon_R|^2}{\alpha}} - 1 \quad (9.36)$$

2766 from a value P_i upstream to an asymptotic value P_f downstream of the resonance.
 2767 This assumes an isolated resonance, crossed at an energy gain ΔE per turn, with a
 2768 crossing speed

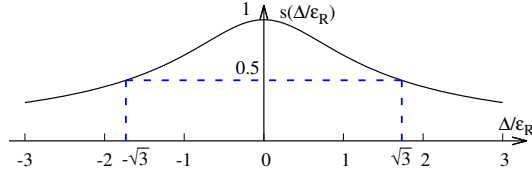
$$\alpha = G \frac{d\gamma}{d\theta} = \frac{1}{2\pi} \frac{\Delta E}{M} \quad (9.37)$$

2769 *Spin precession axis. Resonance width*

2770 Consider the spin vector $\mathbf{S}(\theta) = (S_\eta, S_\xi, S_y)$ of a particle in the laboratory frame,
 2771 with θ the orbital angle around the accelerator. Introduce the projection $s(\theta)$ of \mathbf{S}
 2772 in the median plane

$$s(\theta) = S_\eta(\theta) + jS_\xi(\theta) \quad (\text{and } S_y^2 = 1 - s^2) \quad (9.38)$$

2773 **Fig. 9.17** Modulus of the
 2774 horizontal spin component.
 2775 $s = 1/2$ at distance $\Delta =$
 $\pm\sqrt{3}\epsilon_R$ from $G\gamma_R$



2773 It can be shown that in the case of a stationary solution of the spin motion, viz.
 2774 the spin precession axis, s satisfies [22] (Fig. 9.17)
 2775

$$s^2 = \frac{1}{1 + \frac{\Delta^2}{|\epsilon_R|^2}} \quad (9.39)$$

2776 with $\Delta = G\gamma - G\gamma_R$ the distance to the resonance. The resonance width is a measure
 2777 of its strength (Fig. 9.18). The quantity of interest is the angle, ϕ , of the spin
 2778 precession direction to the vertical axis, given by (Fig. 9.18)

$$\cos \phi(\Delta) \equiv S_y(\Delta) = \sqrt{1 - s^2} = \frac{\Delta/|\epsilon_R|}{\sqrt{1 + \Delta^2/|\epsilon_R|^2}} \quad (9.40)$$

2779 On the resonance, $\Delta = 0$, the spin precession axis lies in the bend plane: $\phi = \pm\pi/2$.
 2780 $S_y = 0.99$ (1% depolarization) corresponds to a distance to the resonance $\Delta = 7|\epsilon_R|$,
 2781 spin precession axis at an angle $\phi = \arccos(0.99) = 8^\circ$ from the vertical.

2782 Conversely, given S_y ,

$$\frac{\Delta^2}{|\epsilon_R|^2} = \frac{S_y^2}{1 - S_y^2} \quad (9.41)$$

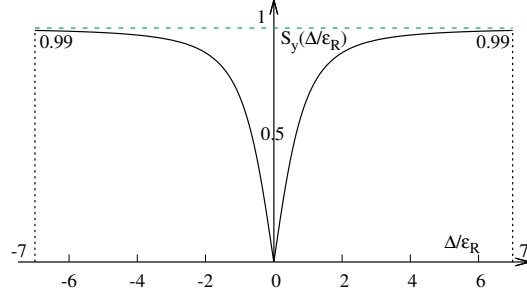


Fig. 9.18 Dependence of polarization on the distance to the resonance. For instance $S_y = 0.99$, 1% depolarization, corresponds to $\Delta = 7|\epsilon_R|$. On the resonance, $\Delta = 0$, the precession axis lies in the median plane, $S_y = 0$

The precession axis is common to all spins, S_y is a measure of the polarization along the vertical axis,

$$S_y = \frac{N^+ - N^-}{N^+ + N^-}$$

2783 wherein N^+ and N^- denote the number of particles in spin states $\frac{1}{2}$ and $-\frac{1}{2}$ respectively.
2784

2785 *Spin motion through weak resonances*

Depolarizing resonances are weak up to several GeV in a weak focusing synchrotron, as the radial and/or longitudinal fields, which stem from a small radial field index and from dipole fringe fields, are weak. Spin motion $S_y(\theta)$ through a resonance in that case can be assumed to satisfy $S_{y,f} \approx S_{y,i}$, with $S_{y,f}$ and $S_{y,i}$ the asymptotic vertical spin component values respectively upstream and downstream of the resonance). As a consequence it can be calculated in terms of the Fresnel integrals [21, 22]

$$C(x) = \int_0^x \cos\left(\frac{\pi}{2}t^2\right) dt, \quad S(x) = \int_0^x \sin\left(\frac{\pi}{2}t^2\right) dt$$

2786 namely, with the origin of the orbital angle is taken at the resonance (Fig. 9.19),

$$\begin{aligned} \text{if } \theta < 0 : \left(\frac{S_y(\theta)}{S_{y,i}}\right)^2 &= 1 - \frac{\pi}{\alpha}|\epsilon_R|^2 \left\{ \left[0.5 - C\left(-\theta\sqrt{\frac{\alpha}{\pi}}\right)\right]^2 + \left[0.5 - S\left(-\theta\sqrt{\frac{\alpha}{\pi}}\right)\right]^2 \right\} \\ \text{if } \theta > 0 : \left(\frac{S_y(\theta)}{S_{y,i}}\right)^2 &= 1 - \frac{\pi}{\alpha}|\epsilon_R|^2 \left\{ \left[0.5 + C\left(\theta\sqrt{\frac{\alpha}{\pi}}\right)\right]^2 + \left[0.5 + S\left(\theta\sqrt{\frac{\alpha}{\pi}}\right)\right]^2 \right\} \end{aligned} \quad (9.42)$$

2787 In the asymptotic limit,

$$\frac{S_y(\theta)}{S_{y,i}} \xrightarrow{\theta \rightarrow \infty} 1 - \frac{\pi}{\alpha}|\epsilon_R|^2 \quad (9.43)$$

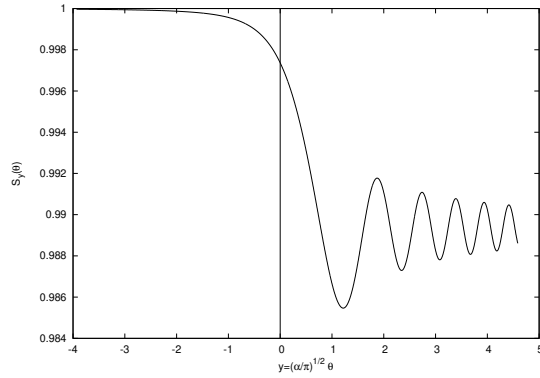


Fig. 9.19 Vertical component of spin motion $S_y(\theta)$ through a weak depolarizing resonance (after Eq. 9.42). The vertical bar is at the location of the resonance, which coincides with the origin of the orbital angle

2788 which identifies with the development of Froissart-Stora formula $P_f/P_i =$
 2789 $2 \exp(-\frac{\pi}{2} \frac{|\epsilon_R|^2}{\alpha}) - 1$ to the first order in $|\epsilon_R|^2/\alpha$. This approximation holds in the
 2790 limit that higher order terms can be neglected: $|\epsilon_R|^2/\alpha \ll 1$.

2791 **9.2 Exercises**

2792 **9.1 Construct Saturne I (weak index) synchrotron. Spin Resonances**

2793 Solution: page 350

2794 In this exercise, Saturne I weak focusing 3 GeV synchrotron is modeled. Spin
 2795 resonances in a weak dipole gradient lattice are studied.

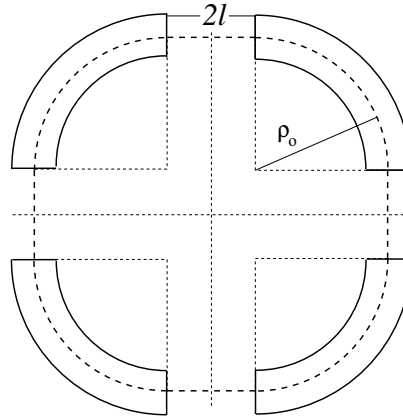


Fig. 9.20 A schematic layout of Saturne I, a $2\pi/4$ axial symmetry structure, comprised of 4 radial field index 90 deg dipoles and 4 drift spaces. The cell in the simulation exercises is taken as a $\pi/4$ quadrant: l-drift/90°-dipole/l-drift

Table 9.1 Parameters of Saturne I weak focusing synchrotron [26]. ρ_0 denotes the reference bending radius in the dipole; the reference orbit, field index, wave numbers, etc., are taken along that radius

| | | |
|---------------------------------|----------|------------------------------------|
| Orbit length, C | cm | 6890 |
| Average radius, $R = C/2\pi$ | cm | 1096.58 |
| Straight section length, $2l$ | cm | 400 |
| Magnetic radius, ρ_0 | cm | 841.93 |
| R/ρ_0 | | 1.30246 |
| Field index n , nominal value | | 0.6 |
| Wave numbers, $\nu_x; \nu_y$ | | 0.724; 0.889 **** verif wrt. simul |
| Stability limit | | $0.5 < n < 0.757$ |
| Injection energy | MeV | 3.6 |
| Field at injection | kG | 0.326 |
| Top energy | GeV | 2.94 |
| \dot{B} | T/s | 1.8 |
| Field at top energy, B_{\max} | kG | 14.9 |
| $B_{\max}\rho$ | T m | 13 |
| Field ramp at injection | kG/s | 20 |
| Synchronous energy gain | keV/turn | 1.160 |
| RF harmonic | | 2 |

2796 (a) Construct a model of Saturne I 90° cell dipole in the hard-edge model, using
 2797 DIPOLE. Use the parameters given in Tab. 9.1, and Fig. 9.20 as a guidance. In order
 2798 to allow beam monitoring, split the dipole in two 45° deg halves. It is judicious to
 2799 take $RM=841.93$ cm in DIPOLE, as this is the reference radius for the definition of
 2800 the radial index. Take an integration step size in centimeter range - small enough to
 2801 ensure numerical convergence, as large as doable for fast multiturn raytracing.

2802 Validate the model by producing the 6×6 transport matrix of the cell dipole
 2803 (MATRIX[IFOC=0] can be used for that, with OBJET[KOBJ=5] to define a proper
 2804 set of paraxial initial coordinates) and checking against theory (Sect. 18.2, Eq. 18.6).

2805 (b) Construct a model of Saturne I cell, with origin at the center of the drift.
 2806 Find the closed orbit, that particular trajectory which has all its coordinates zero in
 2807 the drifts: use DIPOLE[KPOS] to cancel the closed orbit coordinates at DIPOLE
 2808 ends. While there, check the expected value of the dispersion (Eq. 9.26) and of
 2809 the momentum compaction (Eq. 9.28), from the raytracing of a chromatic closed
 2810 orbit - *i.e.*, the orbit of an off-momentum particle. Plot these two orbits (on- and
 2811 off-momentum), over a complete turn around the ring, on a common graph.

2812 Compute the cell periodic optical functions and tunes, using either MA-
 2813 TRIX[IFOC=11] or TWISS; check their values against theory. Check consistency
 2814 with previous dispersion function and momentum commpaction outcomes.

2815 Move the origin of the lattice at a different azimuth s along the cell: verify that,
 2816 while the transport matrix depends on the origin, its trace does not.

2817 Produce a graph of the optical functions (betatron functions and dispersion) along
 2818 the cell. Check the expected average values of the betatron functions (Eq. 9.20).

2819 Produce a scan of the tunes over the field index range $0.5 \leq n \leq 0.757$. RE-
 2820 BELOTE can be used to repeatedly change n over that range. Superimpose the
 2821 theoretical curves $\nu_x(n)$, $\nu_y(n)$.

(c) Justify considering the betatron oscillation as sinusoidal, namely,

$$y(\theta) = A \cos(\nu_y \theta + \phi)$$

2822 wherein $\theta = s/R$, $R = \oint ds/2\pi$.

2823 Find the value of the horizontal and vertical betatron functions, resulting from
2824 that approximation. Compare with the betatron functions obtained in (b).

2825 (d) Launch a few particles evenly distributed on a common paraxial horizontal
2826 Courant-Snyder invariant (vertical motion is taken null), for a single pass through
2827 the cell. Store particle data along the cell in zgoubi.plt, using DIPOLE[IL=2] and
2828 DRIFT[split,N=20,IL=2]. Use these to generate a graph of the beam envelopes.

2829 Using Eq. 9.22 compare with the results obtained in (b). Find the minimum
2830 and maximum values of the betatron functions, and their azimuth $s(\min[\beta_x])$,
2831 $s(\max[\beta_x])$. Check the latter against theory.

2832 Repeat for the vertical motion, taking $\varepsilon_x = 0$, ε_y paraxial.

2833 Repeat, using, instead of several particles on a common invariant, a single particle
2834 traced over a few tens of turns.

2835 (e) Produce an acceleration cycle from 3.6 MeV to 3 GeV, for a few particles
2836 launched on a common $10^{-4} \pi m$ initial invariant in each plane. Ignore synchrotron
2837 motion (CAVITE[IOPT=3] can be used in that case). Take a peak voltage $\hat{V} = 200$ kV
2838 (unrealistic though, as it would result in a nonphysical \dot{B} (Eq. 9.30)) and synchronous
2839 phase $\phi_s = 150$ deg (justify $\phi_s > \pi/2$).

2840 Check the betatron damping over the acceleration range: compare with theory
2841 (Eq. 9.32).

2842 How close to symplectic the numerical integration is (it is by definition *not*
2843 symplectic, being a truncated Taylor series method [27, Eq. 1.2.4]), depends on the
2844 integration step size, and on the size of the flying mesh in the DIPOLE method [27,
2845 Fig. 20]; check a possible departure of the betatron damping from theory as a function
2846 of these parameters.

2847 Produce a graph of the horizontal and vertical wave number values over the
2848 acceleration cycle.

2849 (f) Some spin motion, now. Adding SPNTRK at the beginning of the sequence
2850 will ensure spin tracking.

2851 Based on the file worked out for question (d), simulate the acceleration of a single
2852 particle, through the intrinsic resonance $G\gamma_R = 4 - \nu_Z$, from a few thousand turns
2853 upstream to a few thousand turns downstream. On a common graph, plot $S_y(\text{turn})$
2854 for a few different values of the vertical betatron invariant (the horizontal invariant
2855 value does not matter - explain that statement, it can be taken zero).

2856 (g) Produce a graph of the average value of S_Z over a 200 particle set, as a function
2857 of $G\gamma$, across the $G\gamma_R = 4 - \nu_Z$ resonance. Indicate on that graph the location of
2858 the resonant $G\gamma_R$ values.

2859 Perform this resonance crossing for five different values of the particle invariant:
2860 $\varepsilon_Z/\pi = 2, 10, 20, 40, 200 \mu m$. Compute P_f/P_i in each case, check the dependence
2861 on ε_Z against theory.

2862 Compute the resonance strength, ε_Z , from these trackings.

2863 Re-do this crossing simulation for a different crossing speed (take for instance
2864 $\hat{V} = 10\text{ kV}$) and a couple of vertical invariant values, compute P_f/P_i so obtained.
2865 Check the crossing speed dependence of P_f/P_i against theory.

2866 (h) Show that the previous weak resonance crossings ($P_f/P_i \approx 1$) satisfies
2867 Eq. 9.42. Match the tracking data to the latter to get the vertical betatron tune ν_y , the
2868 location of the resonance $G\gamma_R$, and its strength.

2869 (i) Track a few particles at fixed energy, at distances from the resonance $G\gamma_R =$
2870 $4 - \nu_y$ of up to a $7 \times \epsilon_R$ (this distance corresponds to 1% depolarization).

2871 Produce on a common graph the spin motion $S_Z(\text{turn})$ for all these particles, as
2872 observed at some azimuth along the ring.

2873 Produce a graph of $\langle S_y \rangle|_{\text{turn}}(\Delta)$ (as in Fig. 9.18).

Produce the vertical betatron tune ν_y , the location of the resonance $G\gamma_R$, and its
strength, obtained from a match of these tracking trials to (Eq. 9.40)

$$\langle S_y \rangle (\Delta) = \frac{\Delta}{\sqrt{|\epsilon_R|^2 + \Delta^2}}$$

2874 9.2 Construct the ZGS (zero-gradient) synchrotron. Spin Resonances

2875 Solution: page 374

2876 In this exercise, the ZGS 12 GeV synchrotron is modeled in `zgoubi`. Spin reso-
2877 nances in ZGS wedge focusing zero-gradient synchrotron are studied.

2878 (a) Construct a model of ZGS 45° cell dipole in the hard-edge model, using
2879 DIPOLE. Use the parameters given in Tab. 9.2, and Figs. 9.21, 9.22 as a guidance.
2880 In order to allow beam monitoring, split the dipole in two 22.5° deg halves. Take the
2881 closed orbit radius as the reference $RM=2076\text{ cm}$ in DIPOLE: it will be assumed
2882 that the orbit is the same at all energies⁴. Take an integration step size in centimeter
2883 range - small enough to ensure numerical convergence, as large as doable for fast
2884 multiturn raytracing.

2885 Validate the model by producing the 6×6 transport matrices of both dipole
2886 (MATRIX[IFOC=0] can be used for that, with OBJET[KOBJ=5] to define a proper
2887 set of paraxial initial coordinates) and checking against theory (Sect. 18.2, Eq. 18.6).

2888 Add fringe fields in DIPOLE[$\lambda, C_0 - C_5$], the rest if the exercise will use that
2889 model. Take fringe field extent and coefficient values

$$\lambda = 60\text{ cm } C_0 = 0.1455, C_1 = 2.2670, C_2 = -0.6395, C_3 = 1.1558, C_4 = C_5 = 0 \quad (9.44)$$

2890 ($C_0 - C_5$ determine the shape of the field fall-off, they have been computed from a
2891 typical measured field profile $B(s)$).

2892 (b) Construct a model of ZGS cell accounting for dipole fringe fields, with origin
2893 at the center of the long drift. In doing so, use DIPOLE[KPOS] to cancel the closed
2894 orbit coordinates at DIPOLE ends.

2895 Compute the periodic optical functions at cell ends, and cell tunes, using MA-
2896 TRIX[IFOC=11]; check their values against theory.

⁴ Note that in reality the reference orbit in ZGS moved outward during acceleration [28].

2897 Move the origin at the location (azimuth s along the cell) of the betatron functions
 2898 extrema: verify that, while the transport matrix depends on the origin, its trace does
 2899 not. Verify that the local betatron function extrema, and the dispersion function, have
 2900 the expected values.

2901 Produce a graph of the optical functions (betatron functions and dispersion) along
 2902 the cell.

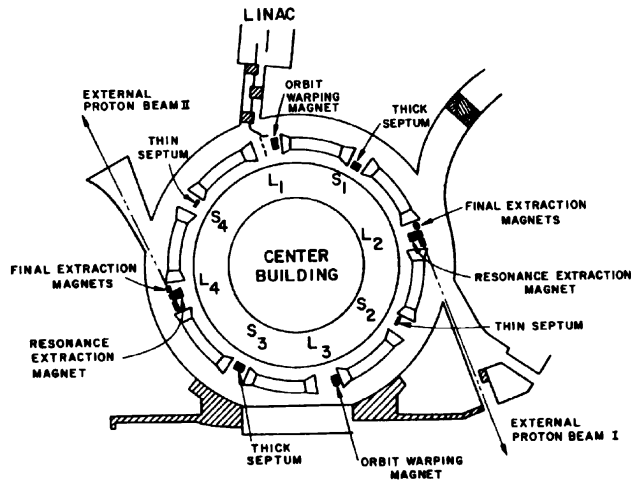


Fig. 9.21 A schematic layout of the ZGS [24], a $\pi/2$ -periodic structure, comprised of 8 zero-index dipoles, 4 long and 4 short straight sections

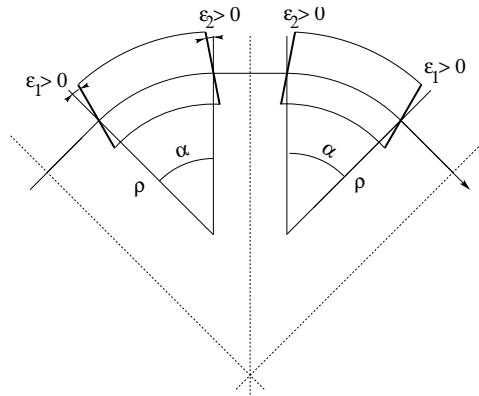


Fig. 9.22 A sketch of ZGS cell layout. In defining the entrance and exit faces (EFBs) of the magnet, beam goes from left to right. Wedge angles at the long straight sections (ϵ_1) and at the short straight sections (ϵ_2) are different

2903 (c) Additional verifications regarding the model.

Table 9.2 Parameters of the ZGS weak focusing synchrotron after Refs. [28, 29][24, pp.288-294,p.716] (2nd column, when they are known) and in the present simplified model and numerical simulations (3rd column). Note that the actual orbit moves during ZGS acceleration cycle, tunes change as well - this is not taken into account in the present modeling, for simplicity

| | | From Refs. [28, 29] | Simplified model |
|---|-------------------|------------------------|--|
| Injection energy | MeV | | 50 |
| Top energy | GeV | | 12.5 |
| $G\gamma$ span | | 1.888387 - 25.67781 | |
| Length of central orbit | m | 171.8 | 170.90457 |
| Length of straight sections, total | m | 41.45 | 40.44 |
| <i>Lattice</i> | | | |
| Wave numbers $\nu_x; \nu_y$ | | 0.82; 0.79 | 0.849; 0.771 |
| Max. $\beta_x; \beta_y$ | m | | 32.5; 37.1 |
| <i>Magnet</i> | | | |
| Length | m | 16.3 | 16.30486 (magnetic) |
| Magnetic radius | m | 21.716 | 20.76 |
| Field min.; max. | kG | 0.482; 21.5 | 0.4986; 21.54 |
| Field index | | | 0 |
| Yoke angular extent | deg | 43.02590 | 45 |
| Wedge angle | deg | ≈ 10 | 13 and 8 |
| <i>RF</i> | | | |
| Rev. frequency | MHz | 0.55 - 1.75 | 0.551 - 1.751 |
| RF harmonic $h = \omega_{rf} / \omega_{rev}$ | | | 8 |
| Peak voltage | kV | 20 | 200 |
| B-dot, nominal/max. | T/s | 2.15/2.6 | |
| Energy gain, nominal/max. | keV/turn | 8.3/10 | 100 |
| Synchronous phase, nominal | deg | | 150 |
| <i>Beam</i> | | | |
| $\varepsilon_x; \varepsilon_y$ (at injection) | $\pi \mu\text{m}$ | | 25; 150 |
| Momentum spread, rms | | | 3×10^{-4} |
| Polarization at injection | % | >75 | 100 |
| Radial width of beam (90%), at inj. | inch | 2.5 | $\sqrt{\beta_x \varepsilon_x / \pi} = 1.1$ |

2904 Produce a graph of the field $B(s)$
 2905 - along the on-momentum closed orbit, and along off-momentum chromatic closed
 2906 orbits, across a cell;
 2907 - along orbits at large horizontal excursion;
 2908 - along orbits at large vertical excursion.
 2909 For all these cases, verify qualitatively, from the graphs, that $B(s)$ appears as
 2910 expected.

(d) Justify considering the betatron oscillation as sinusoidal, namely,

$$y(\theta) = A \cos(\nu_y \theta + \phi)$$

2911 wherein $\theta = s/R$, $R = \oint ds/2\pi$.

2912 Find the value of the horizontal and vertical betatron functions, resulting from
2913 that approximation. Compare with the betatron functions obtained in (b).

2914 (e) Produce an acceleration cycle from 50 MeV to 17 GeV about, for a few particles
2915 launched on a common $10^{-5} \pi$ m vertical initial invariant, with small horizontal
2916 invariant. Ignore synchrotron motion (CAVITE[IOPT=3] can be used in that case).
2917 Take a peak voltage $\hat{V} = 200$ kV (this is unrealistic but yields 10 times faster
2918 computing than the actual $\hat{V} = 20$ kV, Tab. 9.2) and synchronous phase $\phi_s = 150$ deg
2919 (justify $\phi_s > \pi/2$). Add spin, using SPNTRK, in view of the next question, (f).

2920 Check the accuracy of the betatron damping over the acceleration range, compared
2921 to theory. How close to symplectic the numerical integration is (it is by definition
2922 *not* symplectic), depends on the integration step size, and on the size of the flying
2923 mesh in the DIPOLE method [27, Fig. 20]; check a possible departure of the betatron
2924 damping from theory as a function of these parameters.

2925 Produce a graph of the evolution of the horizontal and vertical wave numbers
2926 during the acceleration cycle.

2927 (f) Using the raytracing material developed in (e): produce a graph of the vertical
2928 spin component of the particles, and the average value over that 200 particle set, as
2929 a function of $G\gamma$. Indicate on that graph the location of the resonant $G\gamma_R$ values.

- 2930 (g) Based on the simulation file used in (f), simulate the acceleration of a single
 2931 particle, through one particular intrinsic resonance, from a few thousand turns
 2932 upstream to a few thousand turns downstream.
 2933 Perform this resonance crossing for different values of the particle invariant.
 2934 Determine the dependence of final/initial vertical spin component value, on the
 2935 invariant value; check against theory.
 2936 Re-do this crossing simulation for a different crossing speed. Check the crossing
 2937 speed dependence of final/initial vertical spin component so obtained, against theory.
- 2938 (h) Introduce a vertical orbit defect in the ZGS ring.
 2939 Find the closed orbit.
 2940 Accelerate a particle launched on that closed orbit, from 50 MeV to 17 GeV about,
 2941 produce a graph of the vertical spin component.
 2942 Select one particular resonance, reproduce the two methods of (g) to check the
 2943 location of the resonance at $G\gamma_R = \text{integer}$, and to find its strength.

2944 References

- 2945 1. Veksler, V.: A new method of acceleration of relativistic particles. J. of Phys. USSR 9 153-158
 2946 (1945)
 2947 2. McMillan, E. M.: The Synchrotron. Phys. Rev. 68 143-144 (1945)
 2948 3. Goward, F. K., and Barnes, D. E.: Experimental 8 MeV synchrotron for electron acceleration.
 2949 Nature 158, 413 (1946)
 2950 4. Richardson, J.R., et al.: Frequency Modulated Cyclotron. Phys. Rev. 69: 669 (1946)
 2951 5. Kerst, D. W.: The Acceleration of Electrons by Magnetic Induction.. Phys. Rev., 60, 47-53
 2952 (1941)
 2953 6. Photo saturne I. ***** TB completed **** Archives historiques CEA. Copyright
 2954 CEA/Service de documentation - FAR_SA_N_00248
 2955 7. Photo tranche dipole. Credit: CEA Saclay. ***** TB completed *****
 2956 Archives historiques CEA. Copyright CEA/Service de documentation - FAR_SA_N_02826
 2957 8. Sessler, A., Wilson, E.: Engines of Discovery. A Century of Particle Accelerators. World
 2958 Scientific, 2007
 2959 9. ***** fnal loma linda synch copyrights *****
 2960 10. Endo, K., et al.: Compact proton and carbon ion synchrotrons for radiation therapy. MOPRI087,
 2961 Proceedings of EPAC 2002, Paris, France; pp. 2733-2735.
 2962 <https://accelconf.web.cern.ch/e02/PAPERS/MOPRI087.pdf>
 2963 11. Vostrikov, V.A., et al.: Novel approach to design of the compact proton synchrotron magnetic
 2964 lattice. tupsa17, 26th Russian Particle Accelerator Conference RUPAC2018, Protvino, Russia
 2965 (2018).
 2966 <https://accelconf.web.cern.ch/rupac2018/papers/tupsa17.pdf>
 2967 12. Cohen, D, : Feasibility of Accelerating Polarized Protons with the Argonne ZGS. Review of
 2968 Scientific Instruments 33, 161 (1962).// <https://doi.org/10.1063/1.1746524>
 2969 13. Ratner, L.G. and Khoe, T.K.: Acceleration of Polarized Protons in the Zero Gradient Syn-
 2970 chrotron. Procs. PAC 1973 Conference, Washington (1973).
 2971 http://accelconf.web.cern.ch/p73/PDF/PAC1973_0217.PDF
 2972 14. Bywatwr, J., Khoe, T., et al.: A pulsed quadrupole system for preventing depolarization. IEEE
 2973 Transactions on Nuclear Science (Volume: 20, Issue: 3, June 1973)
 2974 15. Cho, Y., et als.: Effects of depolarizing resonances on a circulating beam of polarized protons
 2975 during or storage in a synchrotron. IEEE Trans. Nuclear Science, Vol.NS-24, No.3, June 1977

- 2976 16. Parker, E.F.: High Energy Polarized Deuterons at the Argonne National Laboratory Zero
2977 Gradient Synchrotron. IEEE Transactions on Nuclear Science, Vol. NS-26, No. 3, June 1979,
2978 pp 3200-3202
- 2979 17. Leleux, G.: Accélérateurs Circulaires. Lecture Notes, INSTN, CEA Saclay (1978)
- 2980 18. Suddeth, D.E., et als.: Pole face winding equipment for eddy current correction at the Zero
2981 Gradient Synchrotron. Procs. PAC 1973 Conference, Washington (1973).
2982 http://accelconf.web.cern.ch/p73/PDF/PAC1973_0397.PDF
- 2983 19. Raugas, A.V. and Wright, A.J.: Betatron tune profile control in the Zero Gradient Synchrotron
2984 (ZGS) using the main magnet pole face windings. Procs. PAC1977 conference, IEEE Trans.
2985 on Nucl. Science, VoL.NS-24, No.3, June 1977
- 2986 20. Floquet, G.: Sur les équations différentielles linéaires à coefficients périodiques. Annales
2987 scientifiques de l'E.N.S. 2e série, tome 12 (1883), p. 47-88.
2988 http://www.numdam.org/item?id=ASENS_1883_2_12_47_0
- 2989 21. Leleux, G.: Traversée des résonances de dépolariation. Rapport Interne LNS/GT-91-15,
2990 Saturne, Groupe Théorie, CEA Saclay (février 1991)
- 2991 22. Méot, F.: Spin Dynamics. Polarized Beam Dynamics and Instrumentation in Particle Accelerators:
2992 USPAS Summer 2021 Spin Class Lectures, Springer (2023)
- 2993 23. Lee, S.Y.: Spin Dynamics and Snakes in Synchrotrons. World Scientific, 1997
- 2994 24. Khoe, T.K., et al.: The High Energy Polarized Beam at the ZGS. Procs. IXth Int. Conf on
2995 High Energy Accelerators, Dubna, pp. 288-294 (1974).
- 2996 25. Froissart, M. and Stora, R.: Dépolariation d'un faisceau de protons polarisés dans un syn-
2997 chrotron. Nucl. Inst. Meth. 7 (1960) 297.
- 2998 26. Bruck H., Debraine P., Levy-Mandel R., Lutz J., Podliasky I., Prevot F., Taieb J., Winter S.D.,
2999 Maillet R., Caractéristiques principales du Synchrotron à Protons de Saclay et résultats obtenus
3000 lors de la mise en route, rapport CEA no.93, CEN-Saclay, 1958.
- 3001 27. Méot, F.: Zgoubi Users' Guide.
3002 <https://www.osti.gov/biblio/1062013-zgoubi-users-guide> Sourceforge latest version:
3003 <https://sourceforge.net/p/zgoubi/code/HEAD/tree/trunk/guide/Zgoubi.pdf>
- 3004 28. Foss, M.H., et al.: The Argonne ZGS Magnet. IEEE 1965, pp. 377-382, June 1965
- 3005 29. Klaisner, L.A., et al.: IEEE 1965, pp. 133-137, June 1965